Development of a Low Aspect Ratio, Helicon Plasma Source using a Flat Spiral Antenna

Taisei MOTOMURA[*1], Kenji TANAKA[*1], Katsuhiko MURAKAMI[*1],
Shunjiro SHINOHARA[*1], Takao TANIKAWA[*2] and Ikkoh FUNAKI[*3]

Abstract

A low aspect ratio, high-density helicon plasma has been produced using a flat spiral antenna in the Large Helicon Plasma Device (LHPD) at Institute of Space and Astronautical Science / Japan Aerospace Exploration Agency (ISAS / JAXA). The experimental method employed and some examples of the experimental results are presented. We describe in detail the behavior of the electron density as a function of the radio frequency (rf) input power. In particular, we focus on the behavior of the threshold power, which strongly depends on the magnetic field strength near the antenna, for the discharge mode transition from Inductively Coupled Plasma (ICP) to Helicon Wave Plasma (HWP). The spatial profiles of the rf wave structures for ICP and HWP are also presented in detail.

Keywords: Helicon wave plasma, High-density plasma, Low aspect ratio plasma, Flat spiral antenna, Inductively coupled plasma.

1. Introduction

A plasma produced by using a helicon wave, helicon plasma [1-4], is widely used in various applications, such as in basic science fields including space plasmas, the development of magnetoplasma rockets and a plasma processing. Using a helicon plasma for plasma production has some advantages of an easy operation and a wide range of operational parameters. In order to fulfill a need for a large volume plasma with a large diameter, a very large volume (up to 2.1 m³), high-density helicon plasma with a large diameter (73.8 cm) has been produced using the Large Helicon Plasma Device (LHPD) at Institute of Space and Astronautical Science / Japan Aerospace Exploration Agency (ISAS / JAXA) [5-10].

In some of the applications mentioned above, e.g., magnetoplasma rockets and a plasma processing, it is desirable to reduce the axial length of the plasma keeping a large diameter, or equivalently, to reduce the aspect ratio A, defined as the ratio between the device diameter and the device axial length. Note that this definition of A is different from that based on the plasma diameter and the axial length: we have employed the former definition for convenience. Using the LHPD at ISAS / JAXA, we have attempted to effectively shorten the plasma column length from 486 cm to as short as 5.5 cm by installing a termination plate inside the chamber [Fig. 1 (a)], reducing A from 6.6 (axial length 486 cm / inner diameter 73.8 cm) to as small as 0.075 (5.5 cm / 73.8 cm). Note that the smallest A attained in the previous experiment other than ours is so far 0.5 [11], which is much larger than our value ($A = 0.075$). The experimental results presented in this paper are taken for $0.4 \leq A \leq 6.6$. The data for the smaller A are presented in Ref. [12].

In this paper, after describing the experimental device and techniques, we present the experimental results of our low aspect ratio ($A \gtrsim 0.5$), high-density helicon plasma. We focus on describing the behaviors of the electron density as a function of the input rf power, the

＊1　Interdisciplinary Graduate School of Engineering Sciences, Kyusyu University
＊2　Research Institute of Science and Technology, Tokai University
＊3　ISAS／JAXA

dependence of the threshold power from Inductively Coupled Plasma（ICP）to Helicon Wave Plasma（HWP）on the magnetic field strength near the antenna, and the spatial profiles of the excited rf wave structures for both of ICP and HWP.

2. Experimental Setup

In this section, we describe the experimental apparatus and the measuring techniques for a low aspect ratio, high-density helicon plasma. In the LHPD at ISAS / JAXA as shown in Fig. 1（a）[5-10], the dimensions of the vacuum chamber are 73.8 cm and 75 cm in inner diameter and in outer diameter, respectively, and 486 cm in axial length. The number of access ports for various probes is 14 on the side walls of the chamber. There are 8 more access ports on the end flanges at both ends. A rotary pump and a turbo molecular pump are connected in series near the antenna region. The base vacuum pressure is $< 5 \times 10^{-6}$ Torr. The axial magnetic field is produced by the 14 main coils and a separate coil which is located at the axial position of $z = 0$ cm. The values of the main coil current, I_m, and the separate coil current, I_s, are typically 50 A and 20 A, respectively. This combination of coil currents produces a uniform axial field of 140 G between $z = 150$ and 300 cm and a non-uniform axial field with a peak value of ~ 50 G in the plasma generation region. We note that it is possible to change the magnetic field configuration near the antenna, $B_A(r)$, by changing I_s, as shown in Fig. 1（b）. For the rest of the paper, the main coil current I_m is fixed at 50 A unless stated otherwise.
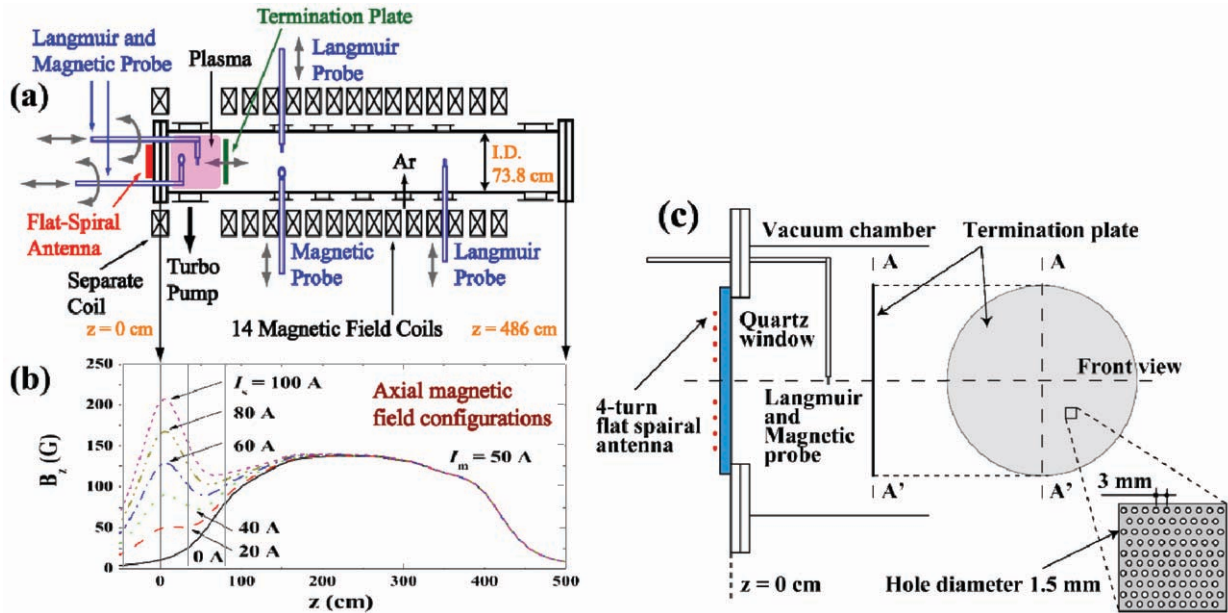

Fig. 1 （a）Schematic drawing of the LHPD. （b）Axial magnetic field configurations for various values of the separate coil current I_s at a radial position of $x = 0$ cm. （c）Schematic drawing of the experimental setup near the flat spiral antenna.

A 4-turn flat spiral antenna [5] of 43 cm in diameter is connected to the rf power supply（maximum power of 5 kW at 7 MHz excitation frequency）through a matching circuit. The antenna is placed outside the vacuum chamber in atmosphere through a quartz window. The rf radiation pattern can be varied by changing the number of spiral turns used for the rf radiation by every 0.5 turns [5]. Note that the antenna excites waves with the $m = 0$ azimuthal mode.

A termination plate, which is movable between $z_E = 5.5$ and 125 cm by using a dc servomotor, is placed in the vacuum chamber, and is electrically floating, where z_E is the axial position of the termination plate. This plate is made of a 0.5-mm thickness stainless steel punching plate. The diameter of each small hole is 1.5 mm, and the center-to-center separation of neighboring holes is 3 mm [see Fig. 1（c）]. A geometrical transparency of the plate is ~ 35 %. The working gas is argon（Ar）with a fill pressure p_{Ar} of $0.75 \sim 15$ mTorr. The gas is fed into the chamber using a needle valve at $z \sim 300$ cm. The electron temperature T_e is typically 3 eV.

Four Langmuir probes are used to measure the spatial profiles of the ion saturation current. Two magnetic probes are used to measure the axial component of the excited rf magnetic field $\tilde{B}_z$.

Two cylindrical Langmuir probes [Fig. 2（a）] and two magnetic probes [Fig. 2（c）] are inserted into the plasma from the end flange（antenna side）. Their probe shafts are bent into an L-shape [see Fig. 1（a）] so that by rotating the probe shafts the probes can radially scan the plasma [the scannable horizontal（or radial）range is $x_p = -35 \sim 35$ cm]. They are also axially movable（axial position $z_p = 0.5 \sim 80$ cm）. One-sided plane probes with 3-mm and 5-mm diameter [Fig. 2（b）] are installed at $z_p = 45$ cm and 336 cm, respectively.
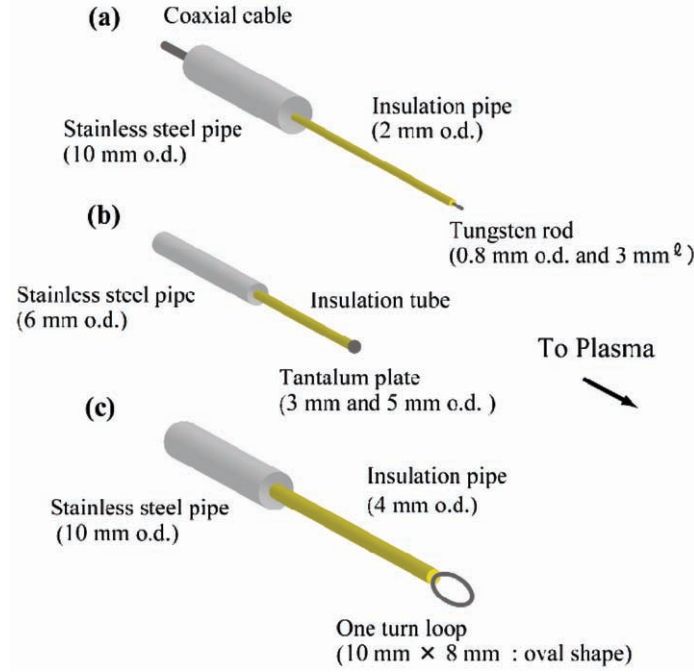

Fig. 2　Schematic drawings of（a）cylindrical and（b）plane Langmuir probes, and
（c）a magnetic probe, respectively.

In order to study the spatial profiles of $\tilde{B}_z$, the rf antenna current $\tilde{I}_A$ is used as a reference signal: the relative amplitude and phase of $\tilde{B}_z$ with respect to $\tilde{I}_A$ are measured. For the measurement of the antenna current, we use a current probe（Pearson 6600）in the matching box, which utilizes a split tank circuit. The forward and reflected rf powers, P_{for} and P_{ref}, respectively, are monitored using a directional coupler. The rf input power P_{inp} to the plasma is defined as P_{for} - P_{ref}. The ratio of the reflected rf power to the forward rf power, P_{ref} / P_{for}, is typically much less than 0.2.

For a cylindrical plasma of uniform density immersed in a uniform dc magnetic field, the axial component of the rf magnetic field, $\tilde{B}_z$, associated with the $m = 0$ helicon wave can be expressed by [13]

$$\tilde{B}_z = Ak_{\perp j}J_0(k_{\perp j}r)\sin(k_{\parallel}z - \omega t), \tag{1}$$

where $k_{\parallel}$ is the parallel wavenumber, J_0 $(k_{\perp j} r)$ is the Bessel function of the first kind, and $k_{\perp j}$ is the j th perpendicular（or radial）wavenumber. The perpendicular and parallel wavenumbers depend on the strength of the background magnetic field, the electron density and the excitation frequency. In calculating the axial profile of $\tilde{B}_z$, various damping effects [13], such as electron-neutral particle collisions, electron-ion collisions and the Landau damping, are taken into account.

3. Experimental Results

3.1　Behavior of the electron density as a function of the input rf power for full-length plasma cases

Figure 3 shows the electron density n_e of a plasma with 486 cm axial length, i.e., the case without the termination plate, as a function of the input rf power P_{inp} for three different values of the separate coil current I_s（= 0, 20 and 60 A）at p_{Ar} = 0.75 mTorr. Here, a Langmuir probe was placed at x_p = 7.5 cm and z_p = 31.5 cm. In the case of I_s = 60 A, the vertical bar at $P_{inp} \sim 1.5$ kW indicates the threshold power,

P_{th}, at which the discharge mode transition from a low density discharge (ICP) mode to a high density (HWP) one occurs.

From Fig. 3, it can be seen that the density jump at P_{th} is quite clear for the $I_s = 60$ A case, while the density change from ICP to HWP for the $I_s \lesssim 20$ A cases is rather gradual. With the increase in the rf power, the electron density increases almost continuously without a clear density jump for the cases of $I_s \lesssim 20$ A. This feature can open up a useful operating regime for our plasma source.

In the high density discharge region, n_e slightly increases with increasing I_s, i.e., the increase in the magnetic field strength near the antenna B_A [see Fig. 1(b)]. The behavior of the threshold power P_{th} as a function of I_s will be described in Sec. 3.3.
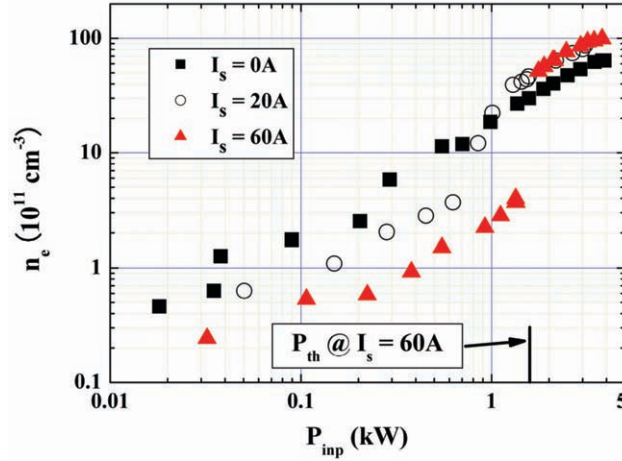
Fig. 3 Electron density n_e as a function of the input rf power P_{inp} with 486 cm (full axial length) for three different values of I_s (= 0, 20 and 60 A) at $p_{Ar} = 0.75$ mTorr. The Langmuir probe was placed at $x_p = 7.5$ cm and $z_p = 31.5$ cm.

3.2 Comparison between the plasma behaviors inside and outside the plasma generation region

Figure 4 compares the rf input power P_{inp} dependences of the electron density n_e outside the plasma generation region with those inside the plasma generation region, the region between the quartz window and the termination plate. Here, the aspect ratio of the plasma generation region, A, is ~ 1.1, i.e., the position of the termination plate z_E is 81 cm. In Fig. 4, the data for two different values of I_s (= 20 A and 60 A) are shown with $p_{Ar} = 0.75$ mTorr. Two Langmuir probes were placed at two different axial positions, $z_p = 45$ cm (inside the plasma generation region) and 336 cm (outside the plasma generation region), on the axis. We expect that the plasma in the plasma generation region leaks into the downstream side of the vacuum chamber through the small holes of the termination plate. As a result, n_e at $z_p = 336$ cm is much lower than that of the antenna side at $z_p = 45$ cm. In the downstream region, i.e., outside the plasma generation region, the rf noise is considered to be low, so that the plasma in this region can be useful for future space plasma simulation experiments, e.g., experiments to simulate nonlinear plasma waves observed in various space plasmas. While the density jump occurs at $P_{inp} = 1 \sim 2$ kW in the plasma generation region (see the data for the case of $z_p = 45$ cm), the density jump is almost non-existent for the data at $z_p = 336$ cm, whose interpretation is left for our future work.

When the helicon wave is excited in the high density discharge mode, the electron density is expected to be nearly proportional to the axial wavenumber of the helicon wave according to the dispersion relation [13]. The dispersion relation of the helicon wave with a uniform spatial density profile and magnetic field [13] is given by

$$k_{\parallel}^2(k_{\parallel}^2 + k_{\perp}^2) = \left(\frac{\omega \omega_{pe}^2}{\omega_{ce}c^2}\right)^2, \tag{2}$$

where ω_{pe}, ω_{ce} and c are the electron plasma angular frequency, the electron cyclotron angular frequency and the speed of light, respectively. According to eq. (2), the axial wavenumber $k_{\parallel}$ is expected to increase as n_e is increased with fixed $k_{\perp}$. In Sec. 3.5, this tendency is discussed by using the results with $A \sim 0.5$.
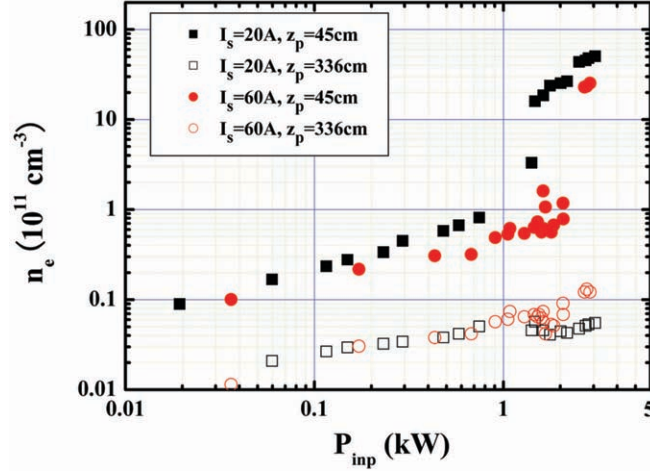
Fig. 4 The rf input power P_{inp} dependence of the electron density n_e outside and inside the plasma generation region with $z_E = 81$ cm and $p_{Ar} = 0.75$ mTorr for $I_s = 20$ A and 60 A.

3.3 Behavior of the threshold power P_{th} as a function of the separate coil current I_s

In this subsection, we will explain how the threshold power P_{th} from the ICP to HWP modes behaves as a function of the separate coil current I_s. In the cases of three different axial lengths, P_{th} increases with the increase in I_s, i.e., the increase in the magnetic field strength near the antenna, B_A（see Fig. 5）. In spite of the non-uniform magnetic field configuration [see Fig. 1（b）], the above observed behavior is very similar to the one observed in the previous work with the uniform magnetic field [14]. Here, the density jump at P_{th} can be understood by the power balance between the power absorbed by plasma, which can be derived from the plasma loading, and the power lost out of plasma [15]. When I_s is fixed, P_{th} is slightly dependent on z_E. As z_E is decreased, n_e in the high density region decreases, indicating the decrease in n_e / P_{inp} with shortening the plasma length.
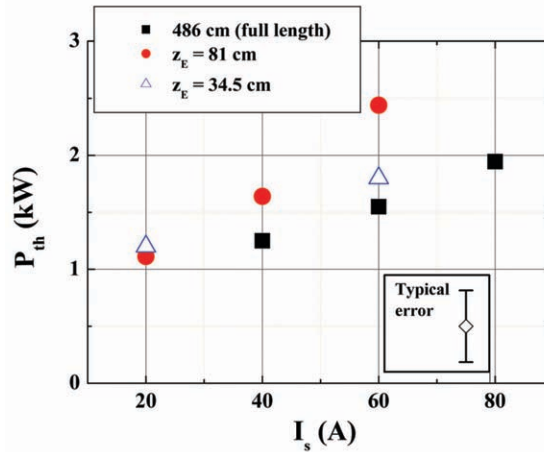

Fig. 5 Threshold power P_{th} as a function of the separate coil current I_s with $z_E = 34.5, 81$ and 486 cm.

3.4 Comparison between the rf field structures in the high and low density regions

In this subsection, we will show that the high density plasma with the external magnetic field is an HWP and the low density plasma without the external magnetic field is an ICP by measuring rf field structures. In order to measure the rf field structures, we measure the excited rf magnetic field $\tilde{B}_z$. Figure 6 shows the amplitude ratio of the excited rf magnetic field to the rf antenna current, $|\tilde{B}_z|$ / $|\tilde{I}_A|$, and the phase difference $\Delta\phi$ between $\tilde{B}_z$ and $\tilde{I}_A$ for plasmas with $z_E = 486$ cm at $p_{Ar} = 0.75$ mTorr. In the figure, the red circles are the data points for a high density HWP（$P_{inp} \sim 2.5$ kW with $I_s = 60$ A）and the square symbols indicate the data obtained for a low density ICP（$P_{inp} \sim 0.5$ kW without magnetic field）. The HWP measurements were performed in the high density region in Fig. 3 with $I_s = 60$ A. For the radi-

al profile measurements of $|\tilde{B}_z| / |\tilde{I}_A|$ and $\Delta\phi$ [Figs. 6(a) and (c)], the magnetic probe location z_p was 21.5 cm for the HWP case and 5 cm for the ICP case.

First, we discuss the axial profiles of the rf wave structure in the low density region from Figs. 6(b) and 6(d). From Fig. 6(b), the e-folding length of $|\tilde{B}_z| / |\tilde{I}_A|$ along the axial direction, L_d, is estimated to be ∼ 2.8 cm in the low density region. The axial skin depth δ_s including the collision effect [16], although ν/ω has a small value of ∼ 0.2 (ν: total electron collision frequency, ω: excitation angular frequency of 7 MHz), can be expressed as $\delta_s = (c / \omega_{pe}) f(\nu)$, where c, ω_{pe} and $f(\nu)$ are the speed of light, the electron plasma angular frequency and a function of the total electron collision frequency, respectively. In our case, the difference between the decay lengths with and without the collision term is small, i.e., $f(\nu) \sim 1.05$. The axial skin depth in the ICP case is calculated to be ∼ 3 cm, which is in agreement with the observed decay length of $L_d \sim 2.8$ cm. In Fig. 6(d), the phase difference in the low density mode only slightly changes in the axial direction for $z \leq 15$ cm. The theoretical result of the axial wavelength, which includes a collision effect [16], is sufficiently long, i.e., the theoretical result of the axial phase change for the ICP case is negligible for $z \leq 15$ cm. Thus, the experimental results of the axial structure of the measured rf wave in the low density mode are consistent with the axial wave structure of an ICP, which is theoretically predicted by including the collisional effect.

Next, we discuss the radial profiles of the rf wave structure in the low density region from Figs. 6(a) and 6(c). From Fig. 6(a), the radial profile of the normalized amplitude, $|\tilde{B}_z| / |\tilde{I}_A|$, in the low density region is much smaller than the one in the high density region. The large phase inversion (the polarity changes at $x \sim \pm 15$ cm) of the low density discharge mode in Fig. 6(c) is very similar to the analytical estimate of the rf magnetic field radiated by the flat spiral antenna in vacuum. Therefore, the experimental results of the radial profiles of the rf wave structure in the low density region is not really associated with the plasma. We conclude that the both radial and axial profiles of the observed rf waves in the low density region are in good agreement with the wave structure of an ICP.

In the high density region, the radial profile of the normalized amplitude $|\tilde{B}_z| / |\tilde{I}_A|$ is clearly different from that in the ICP. From Fig. 6(a), the maximum value of $|\tilde{B}_z| / |\tilde{I}_A|$ in the high density region is about four times larger than that in the ICP. In Fig. 6(b), the decay length along the axial direction in the high density region is considerably longer than that of the ICP case. In Fig. 6(c), the radial profile of $\Delta\phi$ has the propagating wave like structure, which must satisfy the fixed boundary conditions at the radial boundaries of the plasmas. The phase in the high density region changes with the axial position [Fig. 6(d)], and the axial wavenumber is in agreement with the dis-
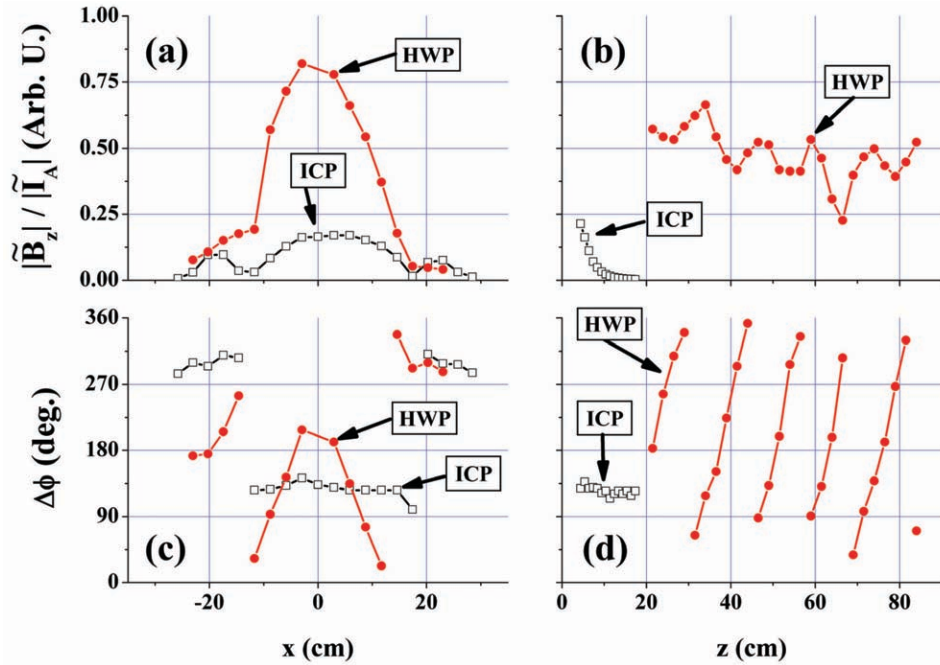

Fig. 6 Comparison between the rf field structures for an ICP ($P_{inp} \sim 0.5$ kW without magnetic field) and an HWP ($P_{inp} \sim 2.5$ kW with $I_s = 60$ A). The radial and axial profiles of the normalized rf amplitude, $|\tilde{B}_z| / |\tilde{I}_A|$, are shown in (a) and (b), respectively. The radial and axial profiles of the phase difference between $\tilde{B}_z$ and $\tilde{I}_A$, $\Delta\phi$, are shown in (c) and (d), respectively. Empty squares and filled circles indicate the data points for the ICP and the HWP, respectively.

persion relation of the helicon wave [13]. In Fig. 6(d), the measured wavenumber of HWP is ~ 0.3 cm^{-1}, while the wavenumber predicted by Eq. (2) is ~ 0.6 cm^{-1}. We believe that this difference mainly arises due to the fact that both electron density and dc magnetic field are non-uniform.

From the measurements, we have found that the radial profiles of our helicon waves can be expressed by a combination of at least two Bessel functions: J_0 $(k_{\perp j} r)$ with $j = 1$ and 2 [17-19]. Also the axial wavenumbers measured are derived from the dispersion relation with the smallest two radial wavenumbers. Additional experimental results of higher order radial profiles $(j \geq 2)$ with a low aspect ratio $(A \sim 1.1)$, high density plasma are described in Ref. 9.

3.5　Wave structures of HWP: a low aspect-ratio case

Figures 7(a) and 7(b) compare the axial waveforms of the HWP in one rf period for two different values of the input rf power. The axial wave forms can be expressed by $|\tilde{B}_z| / |\tilde{I}_A| \sin (\Delta\phi - \omega t)$ [see Eq. (1)]. Note that $(|\tilde{B}_z| / |\tilde{I}_A|)$ and $\Delta\phi$ are the functions of the position and each curve in Fig. 7 corresponds to a waveform at a different t. Also note that the $\tilde{B}_z$ must be a node at the metal termination plate $(z = z_E)$ and an anti-node at the quartz glass window $(z = 0)$ since the axial component of the rf conduction current, j_z, and the rf electric field, E_z, must be zero at an insulator. Because of these boundary conditions, the following condition must be satisfied:

$$L = \frac{1}{4}\lambda_z + \left(\frac{1}{2}\lambda_z\right)p, \quad p = 0, 1, 2, \cdots$$
$$\text{or} \quad n \equiv \frac{L}{\lambda_z} = \frac{1}{4} + \frac{1}{2}p, \quad p = 0, 1, 2, \cdots \tag{3}$$

where L is the plasma column length, λ_z is the axial wavelength, and n is the axial mode number. The axial mode numbers determined from Figs. 7(a) and 7(b) are $3/4$ and $5/4$, respectively. Apparently, the higher rf input power is (or the higher electron density is), the shorter wavelength becomes. This behavior is consistent with that of the helicon dispersion relation, Eq. (2).
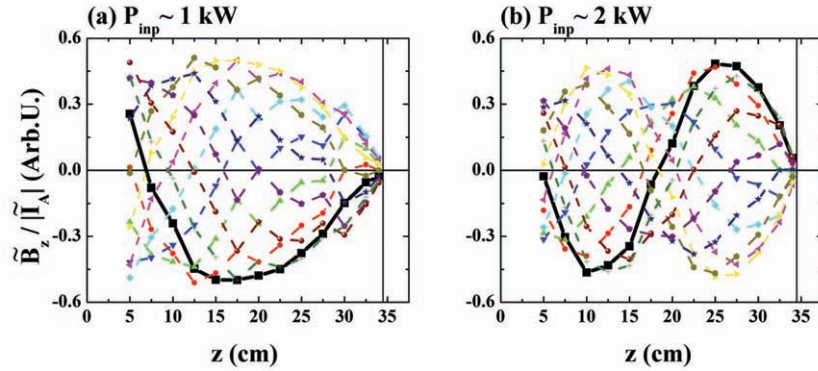

Fig. 7　Axial waveform, $\tilde{B}_z/ |\tilde{I}_A|$, for the rf input power (a) $P_{inp} \sim 1$ kW and (b) $P_{inp} \sim 2$ kW with $z_E = 34.5$ cm (or $A \sim 0.5$), $I_s = 20$ A and $p_{Ar} = 0.75$ mTorr.

3.6　Comparison between the measured wave property and the helicon dispersion relation

In Fig. 8, we compare the measured axial wavenumber of the HWP with the theoretical one using Eq. (2) [13]. The black square, red circle and blue triangle indicate the measured axial wavenumbers determined from Figs. 6, 7(a) and 7(b), respectively.

For the measurements shown in Figs. 7(a) and 7(b), the magnetic field configuration in the plasma generation region is nearly uniform with ~ 50 G [see Fig. 1(b)], while the magnetic field strength is axially non-uniform for the HWP measurement in Fig. 6. In our experiments, the effective plasma radius, a, is approximately $20 \sim 25$ cm. The experimental results of Figs. 7(a) and (b) agree well with the dispersion relation, Eq. (2), with $a \sim 20$ cm. However, in order to recover the parallel wavenumber observed in Fig. 6 using Eq. (2), it is necessary to use $a < 20$ cm, which is too small compared with the experimentally observed plasma radius of ~ 20 cm. We infer from these results that the effects of the non-uniform magnetic field and the radial density profile play important roles in determining the real-world dispersion relation.
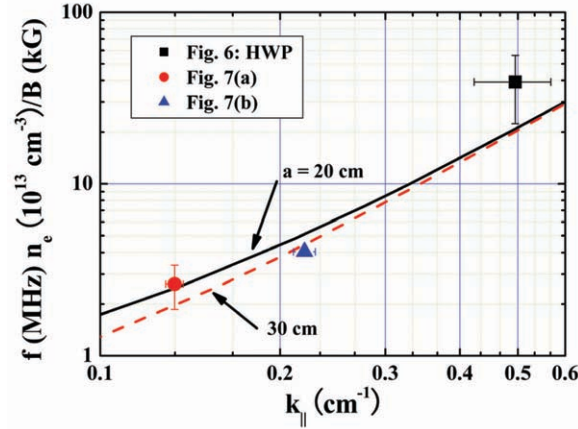
Fig. 8 Comparison between the measured wave properties and the helicon disper-
sion relation, Eq. (2). The solid and dashed curves show the dispersion rela-
tion of the helicon wave determined from Eq. (2) [13] with the effective plas-
ma radius of 20 cm and 30 cm, respectively. The black square, red circle and
blue triangle indicate the wave properties determined from the experiments.

4. Conclusions

We have described the characteristics of large-diameter (73.8 cm), high-density helicon plasmas with various aspect ratios ($A = 0.47 \sim$ 6.6, corresponding to the axial length of $34.5 \sim 486$ cm) produced using a flat spiral antenna. Typical electron density in the plasma generation region is $> 10^{12}$ cm^{-3} in the helicon discharge regardless of the plasma length. The threshold power for the density jump, P_{th}, tends to increase as the magnetic field strength near the antenna ($z \sim 0$ cm) is increased. This tendency persists even if the plasma column length is varied. In the cases of the higher I_s (≥ 60 A) and the longer axial length, P_{th} can be defined more clearly than in the cases of the lower I_s ($\lesssim 20$ A). When $I_s \lesssim 20$ A with the full axial length of 486 cm, it is possible to smoothly vary the plasma density from 10^{10} cm^{-3} to $>$ 10^{12} cm^{-3} by simply changing P_{inp}. This characteristic may open up a new application for our helicon device. In the case of 81 cm axial length, the plasma density outside the plasma generation region changes little even after the occurrence of the density jump inside the plasma generation region.

In the cases of full axial length, we have clearly observed the propagation of the helicon wave along the axial direction in the high density discharge mode, i.e., the HWP discharge, whereas the evanescent wave structure along the axis is found in the low density discharge mode without the background dc magnetic field, i.e., the ICP discharge. The measurements of the wave structures of the HWP with $A \sim$ 0.5, i.e., the case of axial length with 34.5 cm, show that the discrete axial wavenumber increases with the increase in the electron density. This trend is in agreement with the dispersion relation for an HWP with a uniform density profile and a uniform dc magnetic field [13].

Acknowledgements

References

[1] R. W. Boswell, Phys. Lett. **33A**, 457 (1970).

[2] S. Shinohara, Jpn. J. Appl. Phys. **36**, 4695 (1997).

[3] R. W. Boswell and F. F. Chen, IEEE Trans. Plasma Sci. **25**, 1229 (1997).

[4] F. F. Chen and R. W. Boswell, IEEE Trans. Plasma Sci. **25**, 1245 (1997).

[5] S. Shinohara and T. Tanikawa, Rev. Sci. Instrum. **75**, 1941 (2004).

[6] S. Shinohara and T. Tanikawa, Phys. Plasmas **12**, 044502 (2005).

[7]　T. Tanikawa and S. Shinohara, Thin Solid. Films **506–507**, 559 (2006).

[8]　T. Tanikawa and S. Shinohara, *Proc. of the 12th Int. Cong. on Plasma Physics*, (Nice, France, 2004), http://hal.archives-ouvertes.fr/hal-00002013/en/.

[9]　T. Motomura, K. Tanaka, S. Shinohara, T. Tanikawa, K. P. Shamrai, J. Plasma Fusion Res. Ser. **8**, 6 (2009).

[10]　S. Shinohara, T. Hada, T. Motomura, K. Tanaka, Tanikawa, K. Toki, Y. Tanaka and K. P. Shamrai, Phys. Plasmas, **16**, 057104 (2009).

[11]　J. E. Stevens, M. J. Sowa and J. L. Cecchi, J. Vac. Sci. Technol. A 13, 2476 (1995).

[12]　T. Motomura, S. Shinohara, T. Tanikawa and K. P. Shamrai, *Proc. of XXIX International Conf. on Phenomena in Ionized Gases*, Cancun Mexico (2009) PB 9-8.

[13]　F. F. Chen, Plasma Phys. Control. Fusion **33**, 339 (1991).

[14]　S. Shinohara and K. Yonekura, Plasma Phys. Control. Fusion **42**, 41 (2000).

[15]　S. Shinohara and K. P. Shamrai, Plasma Phys. Control. Fusion **42**, 865 (2000).

[16]　S. Shinohara and Y. Kawai, Jpn. J. Appl. Phys. **35**, L725 (1996).

[17]　H. Takeno, Y. Yasaka, O. Sakai and R. Itatani, Nucl. Fusion 35, **75** (1995).

[18]　M. Light, Isaac D. Sudit, Francis F. Chen and Donald Arnush, Phys. Plasmas **2**, 4094 (1995).

[19]　Y. Sakawa, N. Koshikawa and T. Shoji, Plasma Sources Sci. Technol. **6**, 96 (1997).